

# Non-Gaussian modelling and statistical denoising of Planck dust polarization full-sky maps using scattering transforms

J.-M. Delouis<sup>1</sup>\*, E. Allys<sup>2</sup>, E. Gauvrit<sup>1,2</sup>, and F. Boulanger<sup>2</sup>

<sup>1</sup> Laboratoire d’Océanographie Physique et Spatiale (LOPS), Univ. Brest, CNRS, Ifremer, IRD, Brest, France

<sup>2</sup> Laboratoire de Physique de l’École Normale Supérieure, ENS, Université PSL, CNRS, Sorbonne Université, Université Paris Cité, 75005 Paris, France

Wednesday 27<sup>th</sup> July, 2022

## ABSTRACT

Scattering transforms have been successfully used to describe dust polarization for flat-sky images. This paper expands this framework to noisy observations on the sphere with the aim of obtaining denoised Stokes  $Q$  and  $U$  all-sky maps at 353 GHz, as well as a non-Gaussian model of dust polarization, from the *Planck* data. To achieve this goal, we extend the computation of scattering coefficients to the Healpix pixelation and introduce cross-statistics that allow us to make use of half-mission maps as well as the correlation between dust temperature and polarization. Introducing a general framework, we develop an algorithm that uses the scattering statistics to separate dust polarization from data noise. The separation is validated on mock data, before being applied to the SRoll12 *Planck* maps at  $N_{\text{side}} = 256$ . The validation shows that the statistics of the dust emission, including its non-Gaussian properties, are recovered until  $\ell_{\text{max}} \sim 700$ , where, at high Galactic latitudes, the dust power is smaller than that of the dust by two orders of magnitude. On scales where the dust power is lower than one tenth of that of the noise, structures in the output maps have comparable statistics but are not spatially coincident with those of the input maps. Our results on *Planck* data are significant milestones opening new perspectives for statistical studies of dust polarization and for the simulation of Galactic polarized foregrounds. The *Planck* denoised maps will be made available together with results from our validation on mock data, which may be used to quantify uncertainties.

**Key words.** Techniques: image processing, Methods: statistical, Submillimeter: ISM, Cosmology: observations, cosmic background radiation

## 1. Introduction

The cosmic microwave background (CMB) is a prime observational probe for constraining cosmological models (Durrer 2015). Today, with the uncertainties in the CMB temperature spectrum essentially reduced to the cosmic variance (Planck Collaboration V 2020; Planck Collaboration XI 2020), the CMB experiments have shifted their focus to polarization. In particular, accurate measurements of the tensor component ( $B$ -modes) of the polarized signal could provide direct evidence of the inflation period (Guth 1981; Linde 1982). This paramount goal of cosmology is driving the development of ambitious CMB experiments (Abazajian et al. 2016; Ade et al. 2019; LiteBIRD Collaboration et al. 2022), but the potential detection of primordial  $B$ -modes does not only depend on increasing the signal-to-noise ratio on CMB polarization.

The quest for CMB  $B$ -modes is also hampered by instrumental systematic effects (Planck Collaboration III (2020) and polarized foregrounds dominated by Galactic dust emission (BICEP2/Keck Array and Planck Collaborations 2015; Planck Collaboration XI 2020). In this context, the modelling of systematic effects and Galactic foregrounds must advance alongside the sensitivity of the measurements. This is a major challenge because instrumental systematics and Galactic emission are non-Gaussian signals, which in essence are difficult to model. To address this difficulty, the CMB community has been investing much effort in the development of Galactic emission models (Delabrouille et al. 2013; Thorne et al. 2017; Vansyngel et al. 2017; Martínez-Solaache et al. 2018; Zonca et al. 2021; Hervías-Caimapo & Huppenberger 2022) combined with instruments models to produce end-to-end simulations of the data, as done e.g. for *Planck* (Planck Collaboration III 2020). Data sim-

ulations are essential to marginalise the inference of cosmological parameters on the nuisance signals and correct for bias (e.g., Vacher et al. 2022), and to perform Likelihood-Free Inference methods (Planck Collaboration Int. XLVI 2016; Alsing et al. 2019; Jeffrey et al. 2022).

Non-Gaussianity is an important characteristic of Galactic foregrounds. To account for it, several authors have introduced machine learning algorithms (Aylor et al. 2020; Krachmalnicoff & Puglisi 2021; Petroff et al. 2020; Thorne et al. 2021), but these methods need to be trained. Thereby their use is hindered by the difficulty of building relevant training sets. Magnetohydrodynamics (MHD) simulations of the interstellar medium (Kritsuk et al. 2018; Kim et al. 2019; Pelgrims et al. 2022) are useful to develop the methodology but they are far from reproducing the statistics of dust polarization with the accuracy required for CMB components separation.

Another approach to model Galactic foregrounds is to rely on Scattering Transform statistics. These statistics were introduced in data science to discriminate non-Gaussian textures (Mallat 2012; Bruna & Mallat 2013; Cheng & Ménard 2021a), and they have since been applied to dust emission maps computed from MHD simulations (Allys et al. 2019; Regaldo-Saint Blancard et al. 2020; Saydjari et al. 2021). Promising results have also been obtained on various astrophysical processes, as large scale structures density field and galaxy surveys (Allys et al. 2020; Eickenberg et al. 2022; Valogiannis & Dvorkin 2022a,b), weak-lensing convergence maps (Cheng et al. 2020; Cheng & Ménard 2021b), and 21cm data of the epoch of reionization (Greig et al. 2022). To construct these statistics, convolutions of the input image with wavelets over multiple oriented scales are combined with non-linear operators that allow to efficiently characterize interactions between scales.

One notable advantage of the scattering transforms is that generative models reproducing quantitatively the non-Gaussian

\* Corresponding author: J.-M. Delouis, jean.marc.delouis@ifremer.fr

structures of a given process can be constructed from a small number of realizations of this process, which can be even a single image (Bruna & Mallat 2019; Allys et al. 2020). This could allow to construct Galactic dust models directly from observational data. For this purpose, the *Planck* data are a key observational input. They have been used both as a template of the dust sky and to model the spectral energy distribution of dust emission (Thorne et al. 2017; Zonca et al. 2021). However, for polarization, data noise is a severe limitation that must be circumvented. A new direction was opened by Regaldo Saint-Blancard et al. (2021) who introduced an algorithm successfully using scattering statistics to separate dust emission from data noise. They applied it to flat-sky *Planck* Stokes images at 353 GHz. Their method exploits the very different non-Gaussian structure on the sky of dust emission compared to the data noise. An iterative optimization on sky pixels yields denoised maps and a generative model of dust polarization.

This paper aims to extend the innovative approach of Regaldo Saint-Blancard et al. (2021) to the sphere and to apply it to all-sky *Planck* polarization maps. Our scientific motivation is to obtain denoised *Planck* Stokes maps that may be used for the modelling of the dust foreground to CMB polarization. For the astrophysics of dust polarization, the signal-to-noise ratio limits the range of angular scales accessible to study (Planck Collaboration XII 2020). Thus, our work is also a valuable contribution to statistical studies of dust polarization at high Galactic latitudes.

Our data objective involves several challenges. The scattering coefficients must be computed on all-sky maps in Healpix format. The algorithm used to separate dust and data noise must accommodate variations in the dust statistics over the sky. The computing time required to compute the scattering coefficients and the map optimization must be kept manageable. Within this framework, we developed cross-scattering coefficients to make optimal use of the available data, especially complementary half-mission maps. In doing this, we extend the commonly use of cross-power spectra to statistics that encode non-Gaussianity. Indeed, the cross-correlation of *Planck* maps with independent noise realizations facilitates the denoising. It also allows us to take into account the *TE* and *TB* correlation of dust polarization (Planck Collaboration XI 2020).

The paper is organized as follows. Section 2 introduces the cross-scattering statistics, the algorithm and the loss functions from a generic starting-point. Our method is validated on mock data (Sect. 3) before being applied to the *Planck* maps (Sect. 4). Applications and perspectives for future work are discussed in Sect. 5. The paper results are summarized in Sect. 6. Additional figures are presented in Appendix A.

## 2. CWST and dust/noise components separation

We introduce our method in Sect. 2.1, before presenting the cross-scattering transform on the sphere in Sect. 2.2. Next, we describe the algorithm we use to perform the components separation between dust polarization and data noise (Sect. 2.3).

### 2.1. Introduction

The present study aims to characterize the statistical properties of the polarized dust emission from noisy *Planck* all-sky maps in Healpix (Górski et al. 2005). We ignore the CMB, which can be either removed or neglected, and address this problem as a separation between two components: dust emission and data noise.

We choose to work with SRoll2 *Planck* polarization maps at 353 GHz (Delouis et al. 2019). We convert the all-sky Stokes *Q* and *U* maps into *E* and *B* maps, and apply our method to the latter because they are independent scalars that do not depend on the chosen reference frame. This transformation being non-local, signal from the brightest areas in the Galactic plane contaminate the *E* and *B*-maps at high Galactic latitude. Thus, to display the results we transform the denoised *E* and *B*-maps back to *Q* and *U*. In doing so, we also conform to the standard way of representing the polarised sky. In practice, we experimented the use of *E* and *B* is better for the present work.

Our data processing is the same for *E* and *B* maps. In each case, we have access to a full-mission map *d*, and two half-missions *d*<sub>1</sub> and *d*<sub>2</sub>. The half-missions maps are computed from respectively the first and second part of the mission, making their noises and time variable instrumental systematics mostly independent. These maps can be written as a sum of the dust emission *s* and three different noise realisations, that we call respectively *n*, *n*<sub>1</sub> and *n*<sub>2</sub>. One has for instance

$$d = s + n, \quad (1)$$

for the full mission, and

$$d_1 = s + n_1, \quad (2)$$

for the first half mission. We assume that the noises for the two half-missions can be considered statistically independent, at least for  $\ell > 30$  (see for instance Delouis et al. (2019)). Thanks to a simulation effort, we also assume that we have access to a large number of realistic noise maps. The SRoll2 dataset contains for instance an ensemble of 500 ( $\tilde{n}, \tilde{n}_1, \tilde{n}_2$ ) associated triplets of maps (Delouis et al. 2019), which can be used to simulate the noises of the full-mission and of both half-missions of *E*, *B*, and *T* maps. Finally, we also have access to an intensity map, that we label *T*, and that will be used to characterize the statistical dependency between polarized and total intensity dust emission. The details of the different data used and the associated assumptions will be discussed in Sec. 3 and 4.

To obtain the statistical properties of the polarized dust emission, we will perform a components separation of the dust and noise maps, using their different non-Gaussian characterization as a lever arm (Regaldo-Saint Blancard et al. 2020). This components separation generates a new dust maps  $\tilde{s}$  from a gradient descent with an ensemble of statistical constraints built from Cross Wavelet Scattering Transforms (CWST) between different maps. The statistics of the polarized dust map *s* is then estimated from this  $\tilde{s}$  map. In the following, we call FoCUS this components separation method, as Function Of Cleaning Using Statistics.

### 2.2. Cross Wavelet Scattering Transform

Scattering Transforms (ST) are a recently developed type of non-Gaussian summary statistics (Mallat 2012; Bruna & Mallat 2013). They are inspired from convolutional neural networks, but do not need any training stage to be computed (*i.e.*, the function to compute the statistics from a set of data can be written explicitly, and do not need to be learnt). They thus benefit for the low-variance efficient characterization typical to neural networks, but give some level of interpretability through their explicit mathematical form. Several sets of ST statistics have been constructed, as the Wavelet Scattering Transform (WST Allys et al. (2019); Regaldo-Saint Blancard et al. (2020), or the Wavelet Phase Harmonics (WPH Mallat et al. (2018); Allys et al. (2020)). The construction of the ST statistics relies

on two main features: scales separation (through wavelet transforms), and characterization of the interaction between scales using non-linearity (as modulus, ReLU, or phase acceleration). The Cross Wavelet Scattering Transform (CWST), introduced in this paper, is a new type of ST cross-statistics constructed for data defined on the sphere. It is an extension of the WST, to which it boils down when use as auto-statistics.

The first building block of the CWST transform is a wavelet transform allowing fast computation directly on HealPix data. For this purpose, we introduced a very simple multi-resolution wavelet transform defined from four 3x3 complex kernels, which are used to compute convolutions with HealPix maps at different resolutions. These kernels, which are called  $\tilde{\psi}_{j,\theta}$  with  $\theta$  between 1 to 4, are plotted in Fig. 1.

The different wavelets  $\psi_{j,\theta}$  are labeled by a integer scale  $j$  going from 0 to  $J - 1$ , and by a integer angle  $\theta$  going from 1 to  $L$  (associated to a  $(\theta - 1) \cdot \pi/L$ ), for a total of  $J \cdot L$  wavelets. The present work on  $N_{\text{side}} = 256$  map uses  $J = 8$  and  $L = 4$  (since the four  $\tilde{\psi}_{j,\theta}$  kernels define 4 orientations). The wavelet transform for  $j = 0$  is obtained through the convolution of the input map in Healpix with the  $\tilde{\psi}_{0,\theta}$  kernels. The wavelet transform for  $j = 1$  is then obtained by first sub-sampling the input map by computing 2x2 mean, thanks to the Healpix nested indexing property, and computing again the convolutions with the  $\tilde{\psi}_{0,\theta}$  kernels. By repeating this process, one can compute convolutions up to scales  $j = J - 1$ .

As the  $\tilde{\psi}_{0,\theta}$  kernels have a 2 pixels wavelength, the characteristic pic multipole probed by the wavelet transform at scale  $j$  is  $\ell \approx 512 \cdot 2^{-j}$ . Indeed, starting from an initial resolution of  $N_{\text{side}} = 256$  at  $j = 0$ , the resolution on which the convolution is done at  $j > 0$  is  $N_{\text{side}} = 256 \cdot 2^{-j}$ . One also sees that the initial value of  $N_{\text{side}}$  obviously limits the number of scales which can be considered: here  $j = 7$ , which correspond to a Healpix map with  $N_{\text{side}} = 2$ .

We are aware of the fact that more refined way to compute wavelet transform on the sphere exist (see e.g., [Leistedt et al. 2013](#); [McEwen et al. 2015, 2018](#)), from which a first implementation of scattering transform on the sphere has already been defined ([McEwen et al. 2021](#)). We have chosen to do this project within our scheme because of its simplicity of use, as well as its computational efficiency for GPU accelerated computations, especially for the implementation of new cross-statistics. We however would like to transition to better wavelets in the future, for which we could expect an improvement of the obtained results.

In the following, we use an index  $\lambda = (j, \theta)$  to describe the oriented scale associated to each  $\psi_\lambda$ , and we keep implicit the fact that they are defined on HealPix maps of different  $N_{\text{side}}$ . The wavelet convolution of an image  $I$  with a  $\psi_\lambda$  wavelet then reads  $I \star \psi_\lambda(p)$ , where  $p$  is the coordinate on the sphere at the corresponding resolution.

The CWST cross-statistics are calculated on two maps  $I_a$  and  $I_b$ . Similarly to the usual WST, the CWST contain two layers of coefficients, which are characterized respectively by one or two oriented scales  $\lambda_i$ . The whole set of statistics, called  $S(I_a, I_b)$ , is thus decomposed in the  $S_1$  coefficients at first layer, and the  $S_2$  coefficients at second layer. Note that when  $I_a = I_b$ , these coefficients boil down to the usual WST coefficients ([Bruna & Mallat 2013](#)).

The coefficients at first order are called  $S_1(I_a, I_b)_{\lambda_1}$ . They are constructed from a product of convolutions of  $I_a$  and  $I_b$  at the

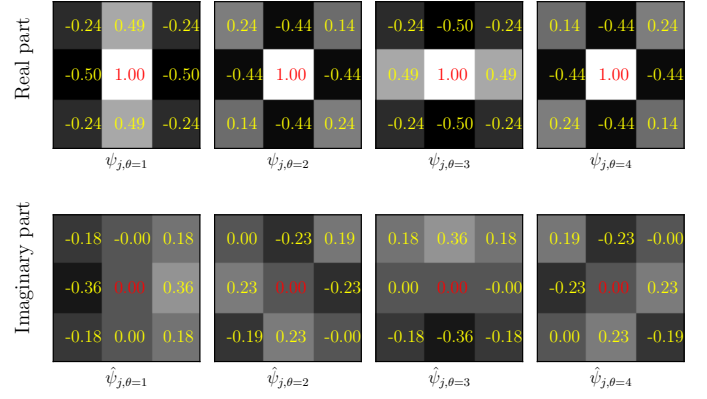


**Fig. 1.** Representation of the four  $\tilde{\psi}_{0,\theta}$  3x3 kernels. The first row shows the real part of the kernel coefficients while the second row shows there imaginary parts.

same  $\lambda_1$  scale:

$$C_1(I_a, I_b)_{\lambda_1}^{\Re} = \text{sign}(\Re(I_a \star \psi_{\lambda_1} \cdot I_b \star \psi_{\lambda_1}^*)) \cdot \sqrt{|\Re(I_a \star \psi_{\lambda_1} \cdot I_b \star \psi_{\lambda_1}^*)|}, \quad (3)$$

and

$$C_1(I_a, I_b)_{\lambda_1}^{\Im} = \text{sign}(\Im(I_a \star \psi_{\lambda_1} \cdot I_b \star \psi_{\lambda_1}^*)) \cdot \sqrt{|\Im(I_a \star \psi_{\lambda_1} \cdot I_b \star \psi_{\lambda_1}^*)|} \quad (4)$$

where we considered independently the real and imaginary part of the products of wavelet convolutions, and where  $*$  and  $|\cdot|$  stand respectively for the complex conjugate (acting here on the whole  $I_b \star \psi_{\lambda_1}$  term) and absolute value. The square root allows to recover L1-like norm, which is useful to decrease the variance of the estimators, but increases the bias while computing the correlated information between two noisy data sets.

The  $S_1$  coefficients are then computed from a spatial integration:

$$S_1(I_a, I_b)_{\lambda_1} = \left\langle C_1(I_a, I_b)_{\lambda_1}^{\Re} + i \cdot C_1(I_a, I_b)_{\lambda_1}^{\Im} \right\rangle_{\text{pixels}}, \quad (5)$$

where  $i$  is the imaginary unit, and where the brackets stand for a spatial average on the sphere, which is multiplied by  $2^j$  to have a uniform normalisation<sup>1</sup>. The  $S_1$  coefficients can also be used to compute the statistics of a single map  $I_a = I_b = I$ . In this case, the  $C_{\lambda_1}^{\Im}$  term obviously vanishes, the  $C_{\lambda_1}^{\Re}$  terms boils down to the complex modulus of the  $I \star \psi_{\lambda_1}$  convolution, and one recovers for  $S_1$  the standard WST definition  $S_1 = \langle |I \star \psi_{\lambda_1}| \rangle_{\text{pixel}}$ .

The coefficients at second order are called  $S_2(I_a, I_b)_{\lambda_1, \lambda_2}$ . They are constructed from two positive and negative terms:

$$\begin{aligned} C_{2,+}^{\Re}(I_a, I_b)_{\lambda_1, \lambda_2} &= \left| \psi_{\lambda_2} \star \text{ReLU}(C_1^{\Re}(I_a, I_b)_{\lambda_1}) \right|, \\ C_{2,-}^{\Re}(I_a, I_b)_{\lambda_1, \lambda_2} &= \left| \psi_{\lambda_2} \star \text{ReLU}(-C_1^{\Re}(I_a, I_b)_{\lambda_1}) \right|, \end{aligned} \quad (6)$$

and similarly for the imaginary terms  $C_{2,\pm}^{\Im}$ . The  $S_2$  terms are then obtained through a spatial integration:

$$\begin{aligned} S_2(I_a, I_b)_{\lambda_1, \lambda_2} &= \left\langle \left( C_{2,+}^{\Re}(I_a, I_b)_{\lambda_1, \lambda_2} - C_{2,-}^{\Re}(I_a, I_b)_{\lambda_1, \lambda_2} \right) \right. \\ &\quad \left. + i \cdot \left( C_{2,+}^{\Im}(I_a, I_b)_{\lambda_1, \lambda_2} - C_{2,-}^{\Im}(I_a, I_b)_{\lambda_1, \lambda_2} \right) \right\rangle_{\text{pixels}}. \end{aligned} \quad (7)$$

<sup>1</sup>Meaning that the  $S_1$  coefficients of a white noise are constant across scales.

For these coefficients, one also recover the standard WST definition  $S_2 = \langle ||I \star \psi_{\lambda_1} \star \psi_{\lambda_2}||_{\text{pixel}} \rangle$  when  $I_a = I_b = I$ .

To use an algebraic sum in Eq. (7) allows to easily identify statistical dependencies between processes. Indeed, if the two images are correlated or anti-correlated, we expect the  $C_1(I_a, I_b)$  to be respectively mostly positive or negative, leading to  $S_2$  values of the same sign. On the other hand, if the two images are uncorrelated, we expect  $C_1(I_a, I_b)$  to have similar positive and negative patterns, thus leading to  $S_2$  coefficients of much lower values. In addition, using a convolution with a second wavelet allows to quantify at which scales such a correlation appears, and thus to characterize an interaction between two oriented scales.

### 2.3. Principle of the components separation.

We present here the components separation method between dust polarization and the data noise, that we call FoCUS for Function Of Cleaning Using Statistics. This method consists in generating a new dust map through a gradient-descent in pixel space under several constraints constructed from CWST statistics. In this part, we call  $u$  the dust map which is modified in the gradient descent. This map is initialized by  $d$ , and we call  $\tilde{s}$  its final value, which is the FoCUS dust map. The scientific result of this paper is this dust map, as well as its statistics. As will be discussed in the validation performed in Sec. 3, while the statistics of  $\tilde{s}$  reproduce very well the ones of the unknown  $s$  dust map, its deterministic structures are not reproduced at the smallest scale.

The constraints which are put on the  $u$  map are based on the full and half-mission maps  $d$ ,  $d_1$ ,  $d_2$ , a  $T$  temperature maps, as well as an ensemble of realization of full and half-mission noises  $\{\tilde{n}, \tilde{n}_1, \tilde{n}_2\}$ . The three constraints we aim to impose are obtained from averages over the ensemble of noise realizations. The first constraint is

$$S(d_1, d_2) \simeq \langle S(u + \tilde{n}_1, u + \tilde{n}_2) \rangle_{\tilde{n}}, \quad (8)$$

where the bracket designs an average over the  $\{\tilde{n}_1, \tilde{n}_2\}$  realizations. This constraint enforces the statistics of  $u$  to the statistics of  $s$  estimated from the two half-mission maps. An average over the noise realization is taken in order to evaluate the noise-related bias. The two other constraints we impose are

$$S(d, u) \simeq \langle S(u + \tilde{n}, u) \rangle_{\tilde{n}}, \quad (9)$$

and

$$S(T, d) \simeq \langle S(T, u + \tilde{n}) \rangle_{\tilde{n}}. \quad (10)$$

The first one constrains the cross-statistics between  $u$  and  $d$ , and is useful to ensure that the structures of the denoised  $u$  map are *aligned* with the structures in  $s$ . The second one imposes to keep the same cross-statistics between  $T$  and  $u$  than those estimated from the  $d$  map.

For this last constraint, we choose  $T$  to be the 857 GHz SRoll3 map, which is corrected for large scale systematics present in earlier data releases (Lopez-Radcenco et al. 2021). The choice of 857 GHz instead of the 353 GHz maps avoid correlated noise between the polarization maps  $d$  and the  $T$  map (as they are computed using data from the same detectors for intensity and polarization). A drawback is that the 857 GHz  $T$  map includes a significant contribution from the Cosmological Infrared Background at high Galactic latitudes, but this emission is only very weakly polarized (Feng & Holder 2020; Lagache et al. 2020). Also, the non-negligible spatial variations of the spectral energy distribution of the Galactic dust induce some

decorrelation between the  $T$  maps at 857 and 353 GHz (Delouis et al. 2021). An advantage of our method is that it is not hindered by such effects, since we only impose the denoised map to have the same statistical dependency than the one estimated from the observational data.

In practice, to perform a gradient descent from the above constraints would however be computationally very costly, due to the necessity to compute an average on a large number of noise realisations (300<sup>2</sup>) at each iteration. To avoid it, the noise-induced biases of the CWST statistics are separated on a specific term and estimated only after a certain batch of iteration. The loss term related to the first constraint is thus written

$$\text{Loss}_1 = \left\| \frac{S(d_1, d_2) - S(u, u) - B_1}{\sigma_{S(u+\tilde{n}_1, u+\tilde{n}_2)}} \right\|^2, \quad (11)$$

with

$$B_1 = \langle S(u + \tilde{n}_1, u + \tilde{n}_2) - S(u, u) \rangle_{\tilde{n}}, \quad (12)$$

where  $\|\cdot\|^2$  stands for the square Euclidean norm over the whole set of CWST statistics, and  $\sigma$  stands for the estimated standard deviation of  $\langle S(u + \tilde{n}_1, u + \tilde{n}_2) \rangle_{\tilde{n}}$ . As discussed above,  $B_1$  gives an estimated of the noise-induced bias between  $S(d_1, d_2)$  and  $S(s, s)$ , which is more accurate the closer  $u$  gets to  $s$  during the optimization.

Similarly, the loss terms related to the second constraint yields:<sup>3</sup>

$$\text{Loss}_2 = \left\| \frac{S(d, u) - S(u, u) - B_2}{\sigma_{S(u+\tilde{n}, u)}} \right\|^2, \quad (14)$$

with

$$B_2 = \langle S(u + \tilde{n}, u) - S(u, u) \rangle_{\tilde{n}}, \quad (15)$$

and the one related to the third constraint yields:

$$\text{Loss}_3 = \left\| \frac{S(T, d) - S(T, u) - B_3}{\sigma_{S(T, u+\tilde{n})}} \right\|^2, \quad (16)$$

with

$$B_3 = \langle S(T, u + \tilde{n}) - S(T, u) \rangle_{\tilde{n}}. \quad (17)$$

These losses treat the Galactic signal as an homogeneous process on the sky. However, it is clear that the dust emission has a strong variation in statistical properties with Galactic latitude. To take this into account, the three losses described previously are computed from statistics estimated on different parts of sky, using 5 different standard Planck masks with  $f_{\text{sky}} \in [1.0, 0.73, 0.63, 0.43, 0.27]$  (Planck Collaboration Int.

<sup>2</sup>500 noise realizations were available but only 300 has been used to limit the memory and computing usage. We also checked that adding additional noises seems not to improve the results anymore.

<sup>3</sup>In practice, the numerical experiments we did showed that it was difficult to use a loss term involving a difference between two  $u$  terms, especially in the start of the optimization where  $u_0 = d$ . To avoid this, we modified this loss term, replacing  $S(u, u)$  by  $S(d_1, d_2) - B_1$ , which proved much more efficient. This led to the following loss term:

$$\text{Loss}_2 = \left\| \frac{S(d, u) - S(d_1, d_2) - B_2 + B_1}{\sqrt{\sigma_{S(u+\tilde{n}, u)}^2 + \sigma_{S(u+\tilde{n}_1, u+\tilde{n}_2)}^2}} \right\|^2. \quad (13)$$

XXX 2016). Dust statistics are dominated by the brightest emission within the unmasked sky. Therefore, as the amplitude of the dust emission decreases steadily from the Galactic plane to the poles, the masks allow us to progressively characterize dust polarization from bright to faint regions when  $f_{\text{sky}}$  goes from 1.0 to 0.27. Since in contrast, the noise power is quite homogeneous in Galactic latitude, this also allows us to evaluate the success of the FoCUS algorithm from large to small signal over noise ratio. In practical terms, the masks are taken into account in the averages over sky pixels in Eqs. (5) and (6). Thus, the FoCUS algorithm simultaneously optimizes the three Loss terms for each of the five masks, i.e. in total 15 constraints.

Numerically, the optimization runs for 500 iterations between each computation of the noise-induced biases. The minimisation does not improve much and the change in  $\tilde{s}$  are negligible after this number of iterations. This step is repeated 12 times (6000 iterations in total), at which point the modification of the estimated biases are very small. The total iteration time represents 10 hours on 3 nodes (processor=Intel Xeon E5-2680) with 28 CPU cores, or 2 hours on 3 M100 GPUs. We also note that the optimization was done on  $d - u$  rather than  $u$ , which was more stable and leads to much less oscillations between local minima. We believe that it is due to the fact that the  $d - u$  contamination is close to a Gaussian random field as scales where FoCUS works, whose pixels values can be optimized in a much more independent way.

### 3. Validation of the components separation

In this section, we apply the FoCUS components separation method to mock data to assess its performance. We introduce the mock data in Sect. 3.1, and present the results of the FoCUS run in Sect. 3.2. In Sect. 3.3, we analyze the impact of each of the three terms of the Loss function on the FoCUS output maps.

#### 3.1. Mock data

To build our mock data set, we combine a model of dust polarization maps with noise simulations. We use the dust model, hereafter the Vansyngel model, introduced in Appendix A of Planck Collaboration III (2020). The Vansyngel model was used by both Planck Collaboration III (2020) and Delouis et al. (2019) to build end-to-end simulations of the Planck polarization data at 353 GHz. The total intensity maps is the Planck map at 353 GHz obtained by applying the Generalized Needlet Internal Linear Combination (GNILC) method of Remazeilles et al. (2011) to the 2015 release of Planck HFI maps (PR2). The Stokes  $Q$  and  $U$  maps are built from one realization of the statistical model of Vansyngel et al. (2017). In the model of Planck Collaboration III (2020), the simulation was replaced by the Planck PR2 353 GHz maps near the Galactic plane, and the largest angular scales  $\ell < 20$  of the simulated maps were also replaced by the Planck data (see Planck Collaboration III (2020) for more details).

Away from the Galactic plane and for multipoles  $\ell > 20$ , the statistical properties of the  $Q$  and  $U$  maps are those of the Vansyngel et al. (2017) model. This model is built from a simplified description of the magnetized interstellar medium where the random component of the magnetic field is represented by Gaussian fields. The  $TE$  correlation and  $E/B$  asymmetry correlation are introduced in the model maps in spherical harmonics with random phases. However, the model  $Q$  and  $U$  maps do have some non-Gaussian characteristics that arise from the total intensity map and the modelling of the line of sight integration with

a small number of independent emission layers. As explained in Sec. 2.3, the temperature map used in the third loss term is the SRoll3 map at 857 GHz, even if the  $T$  map used to evaluate the  $TE/TB$  correlations is the one from the Vansyngel model at 353 GHz. This allows us to remain consistent both for testing the FoCUS algorithm and validating the result obtained.

We associate the dust model  $s_m$  (here the  $m$  index is related to modelisation and simulation) with noise maps from the end-to-end SRoll2 dataset (Delouis et al. 2019). Ten noise realizations are added to the dust model to generate ten mock  $d_m$  maps, and 300 additional ones, all independent, are used for the FoCUS optimization. We apply the FoCUS method on the ten  $d_m$  and obtain ten denoised maps  $\tilde{s}_m$ .

#### 3.2. Validation of FoCUS on mock data

We assess the FoCUS algorithm comparing the maps  $\tilde{s}_m$  with the input dust maps in Sect. 3.2.1, and their CWST statistics in Sect. 3.2.2.

##### 3.2.1. FoCUS maps

The top row of Fig. 2 presents three  $Q$  maps, from left to right the noisy mock data ( $d_m$ ), the input dust model ( $s_m$ ) and the FoCUS output  $\tilde{s}_m$ . The bottom row shows the noise map included in  $n_m$ , the noise estimate from FoCUS  $d_m - \tilde{s}_m$  and the residual  $\tilde{s}_m - s_m$ . The FoCUS map  $\tilde{s}_m$  is strikingly less noisy than  $d_m$ . It is also clear from Fig. 2 that the noise estimate  $d_m - \tilde{s}_m$  corresponds to what we expect: a noisy map with large scale patterns close to the one of the true noise. To the eye, the residual map appears noisier where the dust emission is the brightest. Along the Galactic plane, the residuals are larger but they represent a small fraction of the total dust signal. Away from the Galactic plane, one can see that the residuals do not correspond to leftover noise, but mainly result from small displacements of some structures between  $\tilde{s}_m$  and the true map  $s_m$ .

In Fig. 3, we present  $EE$  power spectra of the maps in Fig. 2 for four masks with  $f_{\text{sky}}$  from 0.27 to 0.73. The corresponding  $BB$  spectra are shown in Fig A.1 in A. In both figures, it is remarkable that the power spectra of the FoCUS output  $\tilde{s}_m$  in orange closely follows the true dust spectrum in black in the four plots, down to two orders of magnitude below the noise power for  $f_{\text{sky}} = 0.27$ . The success in reproducing deterministic dust structures is characterised by the spectra of the residual map  $\tilde{s}_m - s_m$  in red. The power of the residual map becomes larger than that of the dust model in black where the  $EE$  power of dust is one tenth of that of the noise. For lower signal-to-noise ratios, the amplitude of the residual spectrum is about twice that of the dust power, which indicates that structures in the FoCUS output map  $\tilde{s}_m$  are not spatially coincident with those in the input map  $s_m$ . We show below that this corresponds to a regime where the recovered structures have the correct statistical properties, but do not reproduce the input data from a deterministic point of view. The presence of such a regime has already been identified in Regaldo-Saint Blancard et al. (2020).

##### 3.2.2. CWST statistics

A main objective of FoCUS is to derive from an observation a statistical model of dust polarization unbiased by data noise. The mock data allow us to assess the success of the algorithm in this regard.

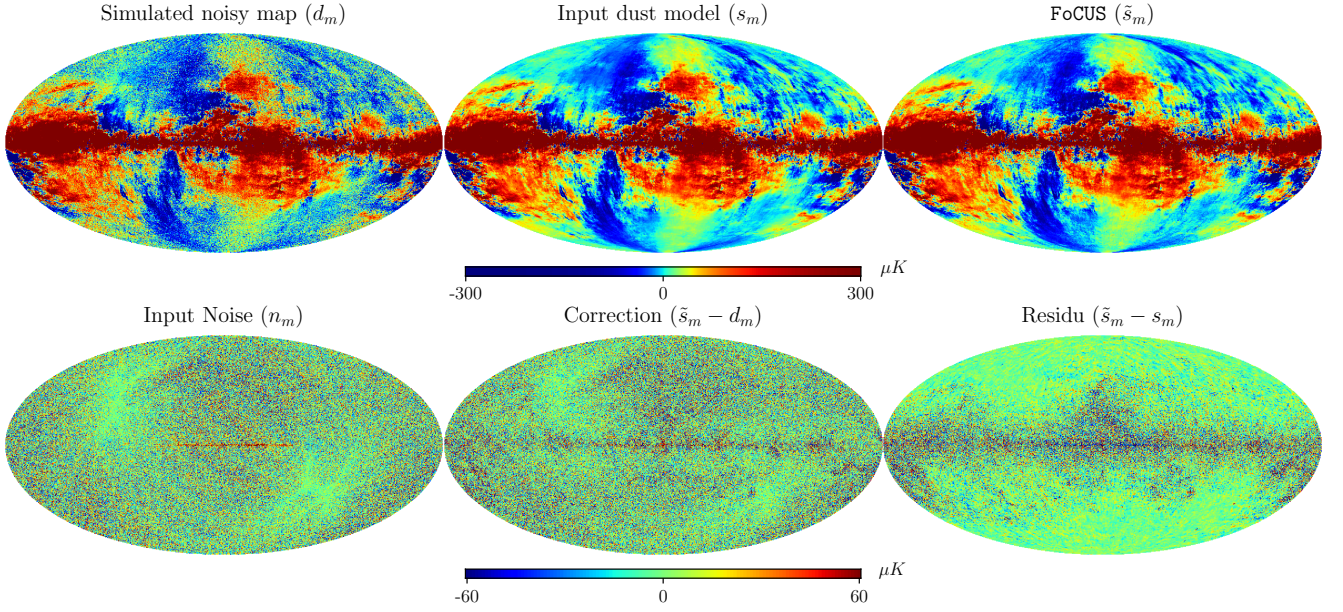


**Fig. 2.** Stokes  $Q$  maps illustrating the validation on mock data. From left to right on the top row: one realization of the noisy mock data, the noise-free Vansyngel model and the result of the FoCUS algorithm. On the bottom line, from left to right the noise map used in the data simulation, the correction found by the FoCUS method and the residual map: the difference between the Vansyngel model and the FoCUS map.

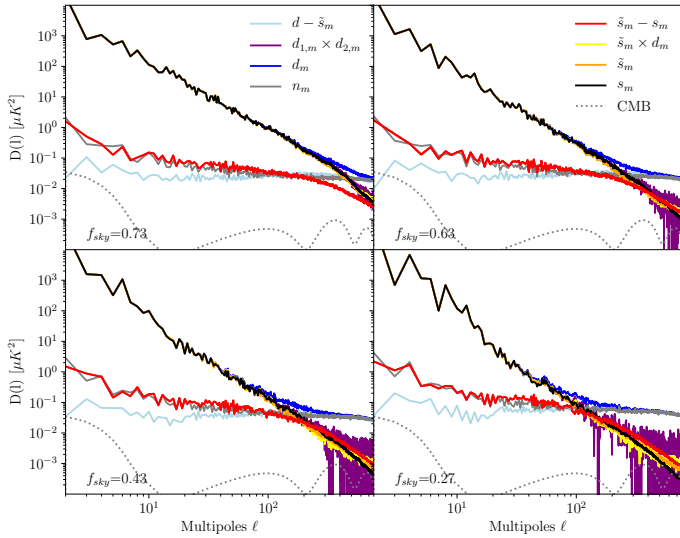


**Fig. 3.** Power spectra of one realization for the FoCUS validation on mock data. The plots show  $EE$  spectra of the dust model ( $s_m$  in black), the noisy mock data ( $d_m$  in blue) and the FoCUS output ( $\tilde{s}_m$  in orange) for four masks with  $f_{\text{sky}}$  from 0.27 to 0.73. The red curve is the power spectrum of the residual map  $\tilde{s}_m - s_m$ . The figure also presents the noise spectrum ( $n_m$ ) and the noise estimate from FoCUS ( $d_m - \tilde{s}_m$ ), as well as cross spectra between half-mission mock maps ( $d_{1,m} \times d_{2,m}$ ) and between  $\tilde{s}_m$  and  $d_m$ . Note that other mock data realisation show very consistent power spectra.

In Figure 4, we compare the CWST coefficients of the FoCUS output map  $\tilde{s}_m$  to those of the mock data  $d_m$  and the noise-free dust model  $s_m$ . As discussed in Sec. 2.2, the CWST coefficients of a single map boil down to the standard WST coefficients studied for instance in Allys et al. (2019). The top row shows the coefficients  $S_1$  averaged over  $\theta_1$  plotted versus scale  $j_1$ , and the bottom row the mean  $S_2$  coefficients averaged over  $\theta_1$  and  $\theta_2$

plotted versus the ratio between the two scales  $j_2 - j_1$ , for  $j_1 = 0$  to 6 from the bottom-right to the top-left.

The statistics of  $d_m$  clearly depart from those of  $s_m$ . As expected, the difference is most noticeable at small scales, as well as for the area of the sky with the lowest signal-to-noise ratio at high Galactic latitudes. For  $f_{\text{sky}} = 0.27$  and  $j_1 = 0$ , the mean  $S_2$  coefficients for  $d$  depart from those of  $s$  for all  $j_2$  but the largest scale. Extracting non-Gaussian statistics of  $s_m$  from the noisy  $d_m$  data down to scale  $j_1 = 0$  is therefore a notable challenge at high Galactic latitudes, where power ratio between the dust signal and noise ratio is down to 1% (see Fig. 3). In this challenging context, the excellent match between coefficients for  $\tilde{s}_m$  and  $s_m$  for all masks demonstrates the remarkable success of the FoCUS algorithm in synthesising maps with the same statistics as the noise-free dust emission.

For the 353 GHz *Planck* data, we however expect some non-negligible bias to appear on the smallest scales probed with  $N_{\text{side}} > 256$ , entering a regime where even the statistical properties of the denoised map begin to differ to those of the true map. This third regime, which has also been observed in Regalado-Saint Blancard et al. (2020), is indeed expected in the limit where the noise has a much higher level than the signal. It could however be possible to use an extrapolated model of the CWST statistics of the dust to describe scales included in this regime.

### 3.3. Impact of each loss term

Our loss functions comprise three terms  $\text{Loss}_1$ ,  $\text{Loss}_2$  and  $\text{Loss}_3$  defined in Eqs. 11, 14 and 16. The mock data allow us to assess the impact of pairwise combinations excluding one of the loss terms for all sky masks on the FoCUS output maps.

Figure 5 include three plots where the input dust model  $s_m$  is drawn in black. All plots are for  $f_{\text{sky}} = 0.63$ . The top plot presents the  $EE$  spectra of the residual maps  $\tilde{s}_m - s_m$  divided by that of  $s_m$ . This ratio quantifies the ability of the FoCUS algorithm to reconstruct structures consistently with the noise-free dust model. The bottom left plot compares the  $TE$  spectrum ob-

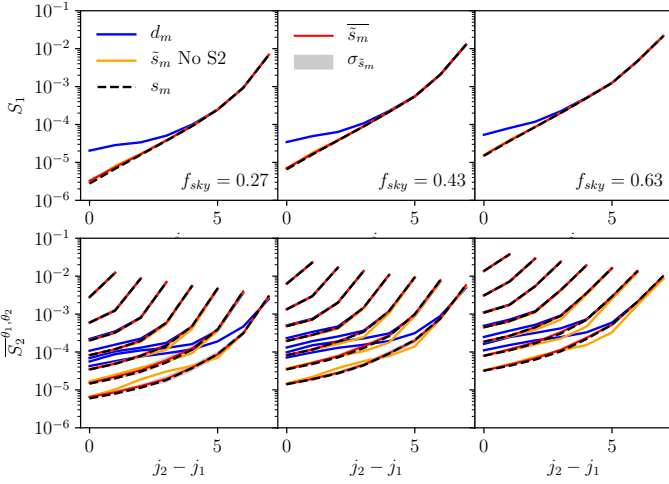


**Fig. 4.** Comparison of CWST statistics. The CWST coefficients of the FoCUS output map  $\tilde{s}_m$  (red solid line) are compared to those of the mock data  $d$  (blue solid line) and the noise-free dust model  $s_m$  (black dashed line). The thicker grey line represents the statistical variance of the FoCUS output estimated from 10 simulations. The top row shows the coefficients  $S_1$  plotted versus scale  $j_1$ , and the bottom row the  $S_2$  coefficients averaged over  $\theta_1$  and  $\theta_2$  plotted versus the ratio between the two scales  $j_2 - j_1$ . The three columns correspond to different Galactic masks.

tained with or without the  $\text{Loss}_3$  term, in red and grey colours. The bottom right plot compares the cross spectra between the FoCUS map  $\tilde{s}_m$  and the mock data  $d_m$  with or without the  $\text{Loss}_2$  term in red and yellow colours, respectively.

In the three plots, the FoCUS output maps  $\tilde{s}_m$  obtained with the complete loss function, drawn in red colour, is the best result, which confirms our choice of combining the three terms of the loss function. The top plot shows that both  $\text{Loss}_1$  and  $\text{Loss}_2$  are essential to minimize the power of the residual maps<sup>4</sup>.  $\text{Loss}_2$  also ensures a faster convergence of the minimization. Furthermore, the bottom right plot shows that  $\text{Loss}_2$  is critical to match the cross spectra  $\tilde{s}_m \times d_m$ .  $\text{Loss}_3$  has only a weak impact on the residual maps, but the bottom left plot shows that it is essential to match the  $TE$  correlation of the dust model, as expected because it constrains the cross statistics between dust polarization and total intensity.

The top plot in Fig. 5 also shows with purple colour the residual power for  $\tilde{s}_m$  maps obtained discarding the  $S_2$  coefficients in the loss function. Comparing the purple and red curves, it is interesting to see that those coefficients only improve by a few tens of percents the residual power. However, yellow curve in Fig. 4 demonstrates that the  $S_2$  coefficients in the loss terms are important to fully recover the non-Gaussian properties of the dust map, as expected.

#### 4. Denoised Planck dust polarization maps

In this section, we use the CWST and FoCUS to separate dust polarization and data noise in *Planck* data. The data we use is in-

<sup>4</sup>We interpret the effect of  $\text{Loss}_2$  as follow. At multipoles between  $10^2$  and  $3 \cdot 10^2$ , this loss allows to recover the deterministic structures which can be characterized from the cross-statistics with the noisy-data. At higher multipoles, these cross-statistics progressively become noise-dominated, and the lever-arm of this loss term to recover deterministic structures decreases.

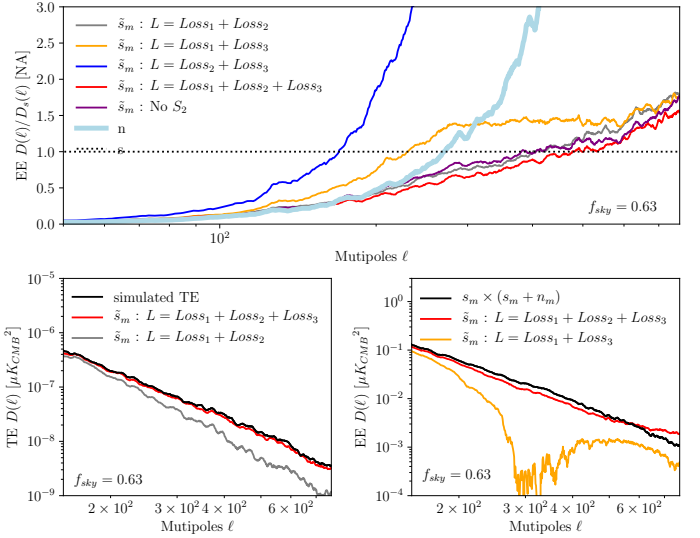


**Fig. 5.** Power spectra of the FoCUS maps for different combinations of the three loss terms  $\text{Loss}_1$ ,  $\text{Loss}_2$  and  $\text{Loss}_3$ . The top plot shows the ratio between the  $EE$  spectra of the residual map,  $s - \tilde{s}_m$ , and the input dust model  $s_m$ . The bottom left plot compares the  $TE$  spectra obtained with or without  $\text{Loss}_3$ , in red and grey colours respectively. The bottom right plot compares the cross spectra between FoCUS map  $\tilde{s}_m$  and the mock data  $d$  with or without  $\text{Loss}_2$ , in red and yellow colours respectively. All of the spectra are binned in  $\ell$  bins with a width  $\Delta\ell = 10$ .

troduced in Sect. 4.1, and the denoised *Planck* polarization maps are presented in Sect. 4.2.

##### 4.1. Input data

We use the *Planck* Stokes  $Q$  and  $U$  maps at 353 GHz from the SRoll2 processing, which corrects instrumental systematics present in the *Planck* Legacy polarization maps of the High Frequency Instrument<sup>5</sup> (Delouis et al. 2019). To obtain dust polarization maps, we subtract the CMB polarization using  $Q$  and  $U$  maps from the SMICA components separation method (Planck Collaboration IV 2020). Over the multipole range we consider, at 353 GHz dust polarization dominates the CMB signal for all sky masks as shown in Fig. 3. Uncertainties on the CMB correction are thus not an issue. As explained in Sec. 2.3, the temperature map used in the third loss is the SRoll3 map at 857 GHz.

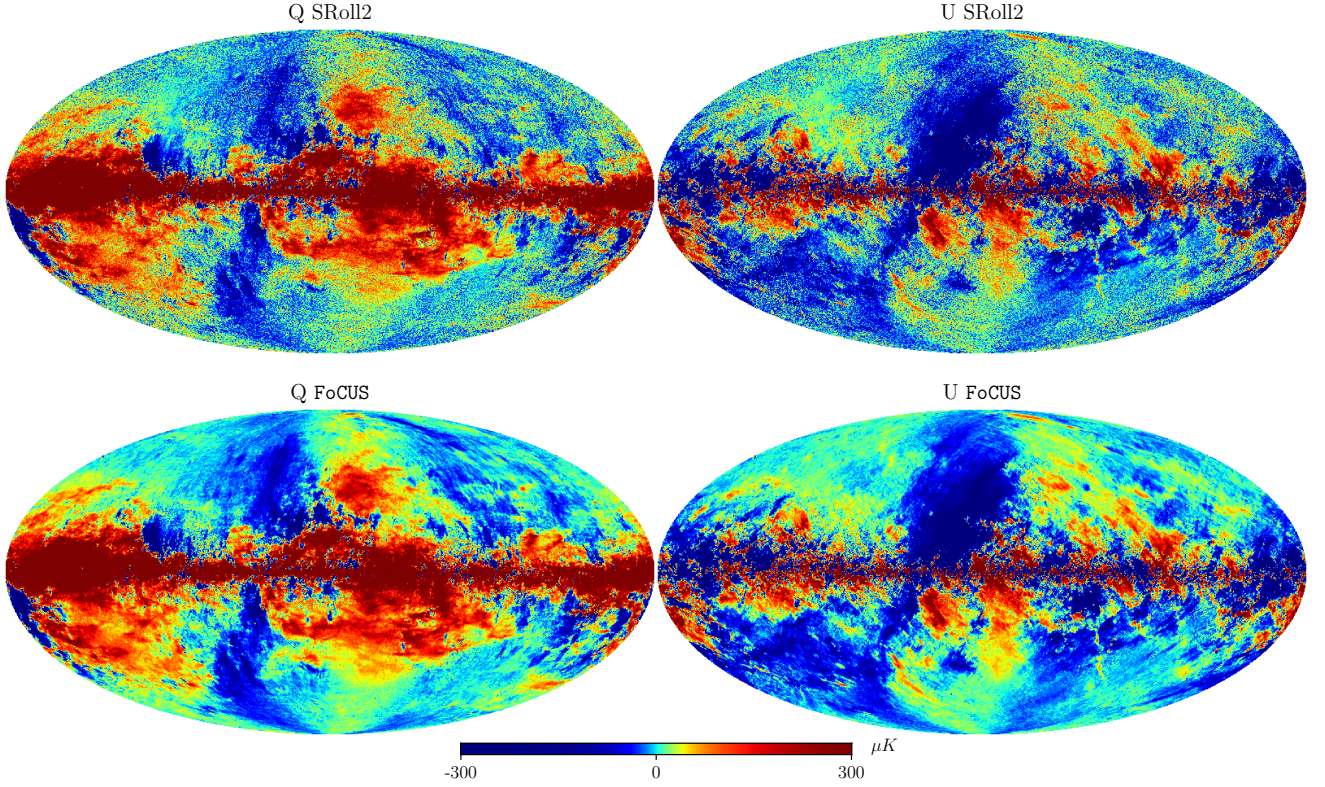
##### 4.2. The FoCUS maps

Figure 6 presents the SRoll2 Stokes  $Q$  and  $U$  maps at 353 GHz (top images) and the result of the FoCUS algorithm (bottom images). The eye-comparison shows that noise has been subtracted without smoothing the map. This is further illustrated in Fig. 7, which zooms on one sky area to allow a detailed comparison with other dust polarization models<sup>6</sup>.

The PySM d1 model map (Thorne et al. 2017; Zonca et al. 2021) includes small scale structure, derived from a random Gaussian field, which appears unrealistic. The Vansyngel maps are constructed from the dust total intensity map. Their textures seem closer to what is statistically expected but the small scales seem to lack of elongated structures. GNILC map shows lack of

<sup>5</sup>The SRoll2 maps are available [here](#).

<sup>6</sup>Note that even without an over-smoothing, the dust map has much less power at small scales than the noise. It is then expected for the denoised map to have a smoother texture.



**Fig. 6.** Stokes  $Q$  and  $U$  maps at 353 GHz for  $N_{\text{side}} = 256$ . The top images present the input *Planck* SRoll2 maps and the bottom ones the corresponding FoCUS maps.

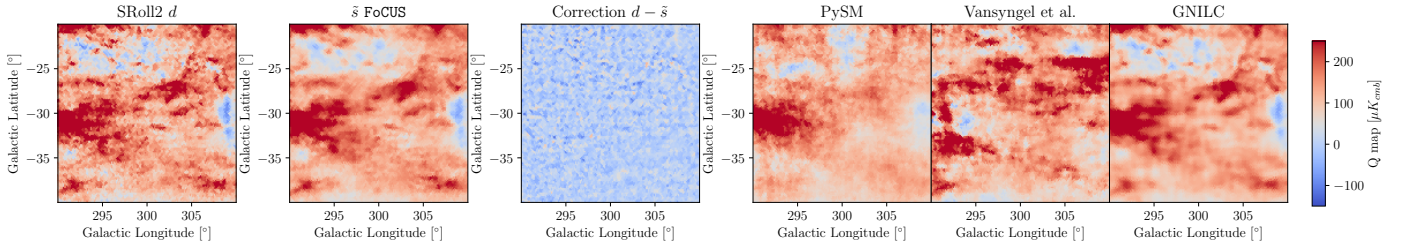


**Fig. 7.** Zoom on a sky region of the  $Q$  map. From the left to right images are the SRoll 2.0 data, the FoCUS map, The correction computed by FoCUS to be applied to the SRoll2.0 map, the PySM d1 model, the (Vansyngel et al. 2017) map and the GNILC map.

small scales. Finally, the FoCUS map shows non-Gaussian elongated structures at all scales, a general characteristics of the diffuse interstellar medium, which our algorithm is able to capture thanks to the use of advanced statistical descriptors and constraints.

Power spectra of the *Planck* data are compared with those of the FoCUS, GNILC, PySM, and Vansyngel maps are compared, for four Galactic masks defined by their corresponding  $f_{\text{sky}}$ , in Fig. 8 and Fig. A.2 (in appendix) for  $EE$  and  $BB$ , respectively. In each figure, plots in the left column present power spectra and those in the right column cross-spectra with the SRoll12 input maps. Each plot includes the cross spectrum between the two SRoll12 half-mission maps ( $d_1 \times d_2$ ) drawn in purple color, as the reference to match because it is a noise-unbiased estimate from the *Planck* data of the spectrum of Galactic dust emission.

In the left column of the two figures, the SRoll12 spectra show the data noise bias over an increasing range of  $\ell$  as  $f_{\text{sky}}$  decreases. It is remarkable that the power spectra of the FoCUS map is consistent with the reference for the four masks, up to multipoles where the signal power is two orders of magnitude

lower than that of the noise. The difference with the GNILC method, which reduces the sky noise at the expense of small scales smoothing, stands out in Fig. 8. The plots also show that the power spectra of the Vansyngel maps deviate somewhat from the *Planck* data, which is a known shortfall of their model.

Plots in the right columns of Fig. 8 and Fig. A.2 present cross-power spectra between models and the SRoll12 maps. Our purpose is to quantify the correlation on the sky between the data and model maps, but we note that our validation of the FoCUS method has shown (see section 2.2) that some correlation may arise from data noise. On these plots, like for those in the left columns, the  $d_1 \times d_2$  cross-power spectra are the references to match. Thus, it is satisfactory to see that the cross-power spectra between the FoCUS and SRoll12 maps is close to  $d_1 \times d_2$  for the four masks. The match is excellent for  $f_{\text{sky}} = 0.73$ . For the other masks we see some loss of correlation at high  $\ell$ , which increases for decreasing  $f_{\text{sky}}$ , i.e. for decreasing signal-to-noise ratio. The correlation is for all masks larger than that measured for the PySM and Vansyngel models. This is expected because

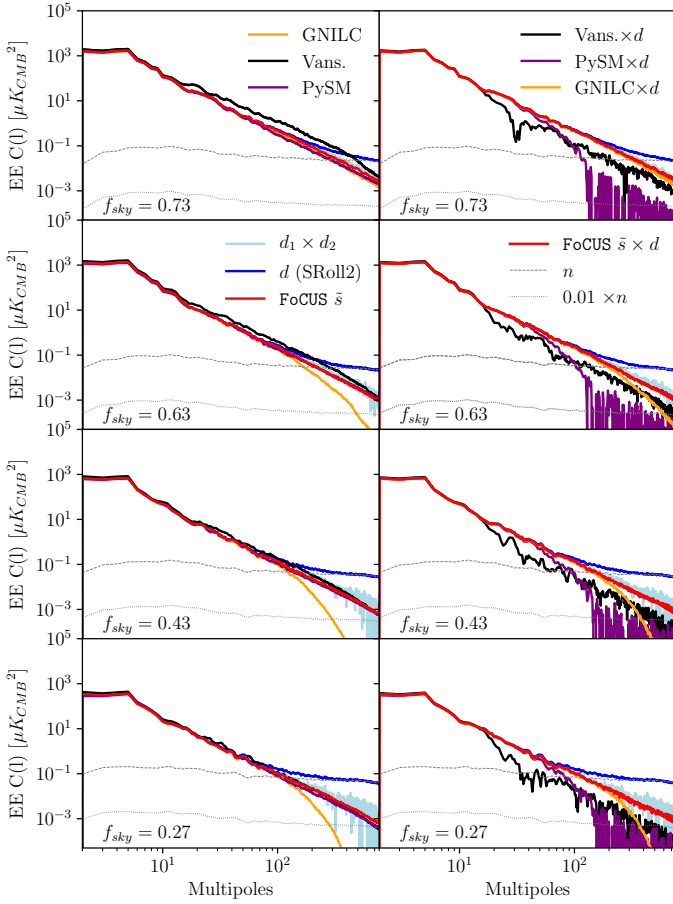


**Fig. 8.** *EE* power spectra (left column) and cross-power spectra (right column) for Galactic masks with  $f_{\text{sky}}=0.27$  (bottom) to 0.73 (top). In each plot, the cross spectrum of the two *Planck* half-mission maps is drawn in purple color. The blue, orange and red curves represent the power spectra of the SRoll2, GNILC and FoCUS maps, respectively. All the spectra are binned over 10 multipoles and normalized by dividing the power with the  $f_{\text{sky}}$  value to keep the scales consistent between the plots.

both these models are constructed with an algorithm that is not designed to preserve correlation with the input data.

#### 4.3. *TE* and *TB* correlation

The *TE* and *TB* correlation are major statistical characteristics of dust polarized emission, determined by the analysis of *Planck* data (Planck Collaboration XI 2020). This important property is difficult to match without learning statistics from data.

In Fig. 9, the *TE* and *TB* cross-power spectra for the SRoll2 and FoCUS maps are compared. The plots show that the two sets of *TE* and *TB* cross-power spectra match, and that the FoCUS algorithm reduces the variance at the highest  $\ell$ . This is a clear success of the FoCUS algorithm. The Fig. 9 also shows that the previous noise removal (see GNILC or (Vansyngel et al. 2017) in orange or black) do not reproduce these correlations.

### 5. Projected applications and perspectives

The *Planck* 353 GHz polarization maps have been extensively used for the astrophysics of dust polarization and the modelling of the Galactic dust foreground to CMB. For both topics, the FoCUS map represents a significant stepping-stone opening new

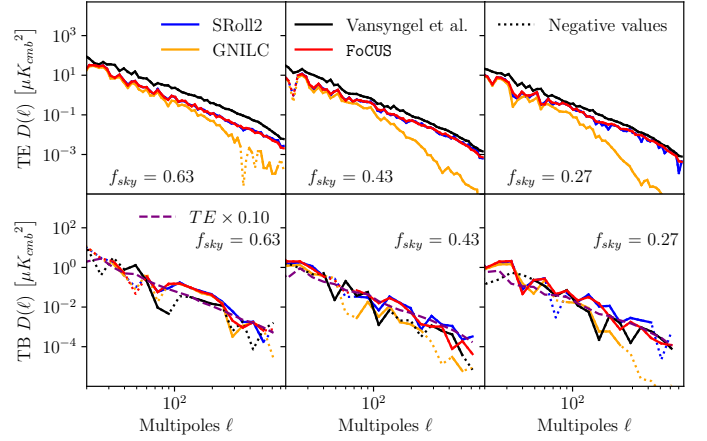


**Fig. 9.** *TE* (top row) and *TB* (bottom row) cross-power spectra of the SRoll2 (blue curves) and FoCUS maps (red curves). The orange and black curves show the same results for the GNILC and Vansyngel maps. Each column corresponds to a different galactic mask. The cross-power spectra are binned in bins of width  $\frac{\Delta\ell}{\ell} = 0.05$  for *TE* and 0.2 for *TB* to reduce the noise variance. Dotted lines represent negative values.

prospects. We illustrate and discuss these perspectives from both the astrophysics and foregrounds viewpoints.

#### 5.1. Astrophysics of dust polarization

For astrophysics, the signal-to-noise ratio of the dust polarization maps statistically conditions the range of angular scales accessible to study. The polarized emission of the diffuse ISM at high Galactic latitudes is too faint to be analyzed at the full 5' angular resolution of *Planck* (see dust power spectra in Planck Collaboration XI (2020)). As a matter of fact, most of the analysis of the dust polarized emission in Planck Collaboration XII (2020) was performed after smoothing the *Planck* maps to 80' and even 160' resolution. The FoCUS maps thus allow us to extend the range of earlier studies. As our data denoising is statistical in nature at scales where signal-to-noise ratio is low, the FoCUS maps are most relevant to statistical studies, in particular those that aim at characterizing statistically the turbulent component of the Galactic magnetic field.

To illustrate this perspective, we use the FoCUS maps to compare the polarization angle dispersion,  $\mathcal{S}$ , and the polarization fraction,  $p$ , as done by Planck Collaboration XII (2020) with the *Planck* Legacy maps.  $\mathcal{S}$ , introduced by Hildebrand et al. (2009) and Planck Collaboration Int. XIX (2015), quantifies the local non-uniformity of the polarization angle patterns on the sky by means of the local variance of the polarization angle map on a scale defined by a lag  $\delta$ . Regions where the polarization angle tends to be uniform exhibit low values of  $\mathcal{S}$ , while regions where the polarization patterns change on the lag-scale exhibit larger values. The polarization fraction,  $p$ , depends on both the orientation of the mean Galactic magnetic field in the Solar Neighborhood and, statistically, on depolarization resulting from changes in the magnetic field orientation along the line of sight (Planck Collaboration Int. XLIV 2016). The trend  $\mathcal{S} \propto 1/p$  observed in the *Planck* data can be reproduced with an analytical model presented in Appendix A of Planck Collaboration XII (2020). The product  $\mathcal{S} \times p$  scales with the degree of randomness of the Galactic magnetic field: the ratio between the dispersion of the turbulent component and the strength of the mean field.

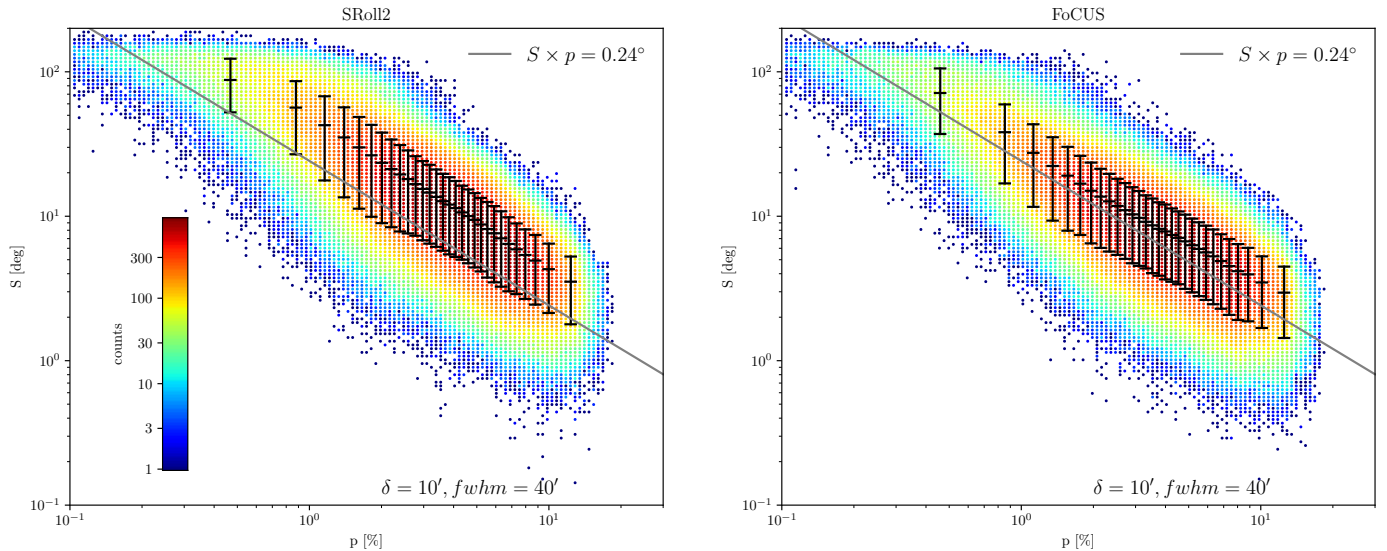


**Fig. 10.** Distribution of the polarization angle dispersion  $S$  and the polarization fraction  $p$  values for the SRoll2 (left panel) and FoCUS (right panel) maps. The data points with error-bars represent the mean value and  $1\sigma$  dispersion of  $S$  within bins of  $p$ . The data binning and representation follows that of Fig. 10 of [Planck Collaboration XII \(2020\)](#). The gray line shows the relation  $S \times p = 0.24^\circ$ , which is expected based on the analytical model of [Planck Collaboration XII \(2020\)](#) for the resolution FWHM=40' we use.

Figure 10 presents plots of  $S$  versus  $p$ , for both the SRoll2 and FoCUS maps, with the same presentation as in the corresponding Figure (also Fig. 10) in [Planck Collaboration XII \(2020\)](#). Figure A.3 presents the corresponding plots for the Vansyngel model. Our maps have a resolution of 40' (FWHM) to be compared with 160' for the plot in [Planck Collaboration XII \(2020\)](#). As in [Planck Collaboration Int. XIX \(2015\)](#), we use a lag equal to one fourth of FWHM, i.e.  $\delta = 10'$ . The model relation for our resolution and lag,  $S \times p = 0.24^\circ$ , is the line drawn in both plots. We see from Fig. A.3 that the noise bias on the  $S$  and  $p$  relation is considerably reduced by the FoCUS algorithm. Given the excellent debiasing obtained on this validation dataset, the FoCUS plot in Fig. 10 suggests that the analytical model of ([Planck Collaboration Int. XIX 2015](#)) only provides an approximate description of the data.

## 5.2. Galactic foregrounds modelling

The modelling of the dust foreground to CMB polarization is the primary motivation of our work. The approach we follow to model dust polarization is novel in some crucial aspects, which we summarize here.

We learn our statistical model from the *Planck* data using a set of summary statistics designed to perform an in-depth characterization of non-Gaussian structures ([Bruna & Mallat 2013](#)). The FoCUS maps include non-Gaussian features that are missed by models making use of Gaussian random fields to describe foregrounds on scales where the *Planck* template maps are noise dominated. This important difference is illustrated in Fig. 11, where ratios between CWST coefficients  $S_2/S_1$ , used as a measure of non-Gaussianity, are compared between the FoCUS PySM and Vansyngel  $E$  maps.

We have applied to all-sky *Planck* maps a statistical components separation that allow us to extend our statistical model of dust polarization down to scales where the dust power is two orders of magnitude smaller than the data noise. For the sky at high Galactic latitudes best suited for deep CMB observations we succeed in modelling dust polarization up to  $N_{\text{side}} = 256$ .

The resolution could be increased by modelling and extrapolating the scale-dependence of CWST coefficients.

The CWST statistics allow us to combine different maps. We have used this possibility to learn from the *Planck* data the correlation between dust total intensity and polarization. Therefore, our FoCUS map reproduces the  $E/B$  asymmetry, the  $TE$  and also  $TB$  correlations, a unique achievement among current dust models illustrated in Fig. 9.

To go further on the modelling of polarized Galactic foregrounds, one main objective will be to extend this analysis to multi-frequency models that take into account the spatial variations of the spectral energy distribution of dust polarization ([Ritacco et al. 2022](#)). For this purpose, it is necessary to properly construct joint multi-channels Scattering Transform statistics, as well as to extend the components separation algorithm to this framework.

## 6. Conclusion

We have applied the scattering transform to *Planck* data in order to derive a non-Gaussian model of dust polarization and produce denoised all-sky dust Stokes  $Q$  and  $U$  maps at 353 GHz. First, we introduced the CWST statistics that we use to characterize the non-Gaussian structure of dust polarization. They extend the computation of scattering coefficients to the Healpix pixelization on the sphere and include cross-statistics that allow us to combine images. Second, we devised the FoCUS algorithm that uses the CWST statistics to separate dust polarization from data noise. FoCUS is validated on simulations of the *Planck* data, before being applied to the SRoll2 *Planck* maps at 353 GHz. The main results of our work are as follows.

The CWST statistics and the FoCUS algorithm allow us to characterize dust polarization down to angular scales where the  $EE$  dust power is two orders of magnitude smaller than that of the data noise. The FoCUS Stokes maps reproduce *Planck* dust polarization power spectra estimated from cross-spectra of half-mission maps over these scales.

Our validation on mock data allow us to compare the FoCUS output map  $\tilde{s}$  with the noise-free input map  $s$ . The spectra of

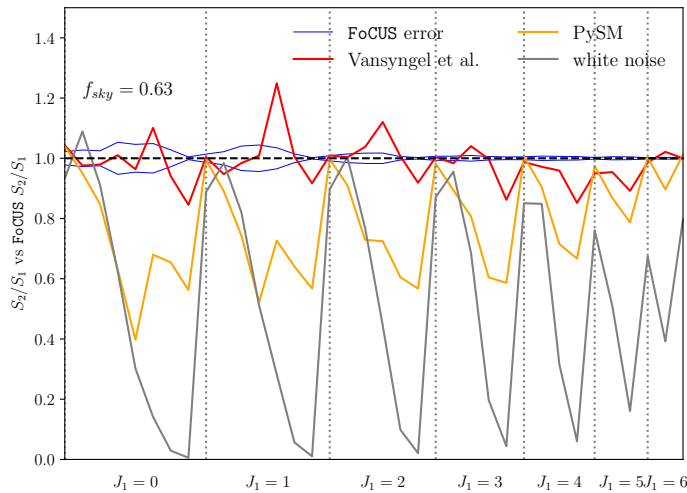


**Fig. 11.** Comparison of the second order  $S_2$  CWST coefficients used as a measure of non-Gaussianity. The  $S_2$  coefficients of  $E$  maps normalized by  $S_1$  are plotted versus scales  $J_1$  and  $J_2$ . The data are ordered by  $J_1$  values and for each  $J_1$  for increasing  $J_2$ . The plot compares  $S_2/S_1$  ratios for a Gaussian map in purple, PySM model in yellow and that of Vansyngel et al. (2017) and the FoCUS map with a black dashed line. All data values are normalized by those of the FoCUS map. The two blue curves shows the uncertainty ( $\pm 1\sigma$ ) on the  $S_2/S_1$  ratio estimated from simulations.

the residual map  $\tilde{s} - s$  becomes larger than that of  $s$  at scales where the  $EE$  dust power is lower than one tenth of the noise power. On these scales, structures in the FoCUS output maps  $\tilde{s}$  have comparable non-Gaussian statistics, estimated in terms of CWST, but are not spatially coincident with those in  $s$ .

The FoCUS Stokes maps at 353 GHz, with a set of residual maps from our mock data analysis quantifying uncertainties, are made available to the community. The FoCUS maps open new prospects for astrophysics and the modelling of the Galactic dust foreground to CMB polarization.

For astrophysics, the signal-to-noise ratio of the dust polarization maps limits the range of angular scales accessible to study. Since our denoising of the data is statistical in nature at scales where the signal-to-noise ratio is low, the gain is in statistical studies. We illustrate this type of applications repeating the *Planck* studies of the anti-correlation between the dispersion of polarization angles and the polarization fraction.

The FoCUS Stokes maps improve on current models of dust polarization in two main aspects. (1) The FoCUS maps include non-Gaussian characteristics of dust polarization, which are missed by models making use of Gaussian random fields to describe foregrounds on scales where the *Planck* maps are noise dominated. (2) The CWST cross-statistics allow us to learn from the *Planck* data the correlation between dust total intensity and polarization. Therefore, our FoCUS map reproduces the  $E/B$  asymmetry and the  $TE$  and  $TB$  correlations, a unique achievement among current dust models used to assess CMB components separation methods.

A clear path to improve our results would be to use state-of-the-art Scattering Transform statistics on the sphere. Following recent works, several improvements of the scattering statistics could be done in the near future. On the one hand, more refined wavelet transforms on the sphere could be used, as discussed in Sec. 2.2. On the other hand, other successful sets of scattering statistics, which give better syntheses on regular 2D grids, could be used. For instance, the Wavelet Phase Harmonics (Allys et al.

2020; Jeffrey et al. 2022) or the more recent representations built from Wavelet Scattering Covariances (Morel et al. 2022; Cheng et al. 2022). However, the main challenge is to make such improvements feasible given the computational and memory costs of the FoCUS algorithm.

On a more general aspect, the CWST statistics and the FoCUS algorithm could be applied to many processes defined on the sphere, including in other area than astrophysics, to leverage and analyze different types of correlated data. Its two main advantages are its ability to efficiently combine different datasets and statistical constraints.

**Acknowledgements.** This work is part of the R & T Deepsee project supported by CNES. The authors acknowledge the heritage of the Planck-HFI consortium regarding data, software, knowledge. This work has been supported by the Programme National de Télédetection Spatiale (PNTS, <http://programmes.insu.cnrs.fr/pnts/>), grant n° PNTS-2020-08 and by the CNRS to the 80 Prime project AstrOcean. FB acknowledges support from the Agence Nationale de la Recherche (project BxB: ANR-17-CE31-0022). The authors thank C. Auclair, S. Cheng, M. Eickenberg, F. Levrier, J. McEwen, S. Mallat, B. Ménard, R. Morel, B. Regaldo and P. Richard for useful discussions.

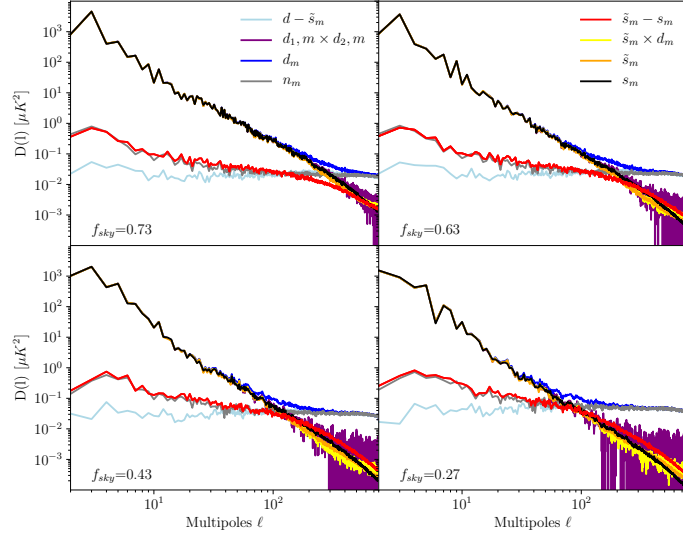
## References

- Abazajian, K. N., Adshead, P., Ahmed, Z., et al. 2016, ArXiv e-prints
- Ade, P., Aguirre, J., Ahmed, Z., et al. 2019, *J. Cosmology Astropart. Phys.*, 2019, 056
- Allys, E., Levrier, F., Zhang, S., et al. 2019, *Astronomy Astrophysics*, 629, A115
- Allys, E., Marchand, T., Cardoso, J. F., et al. 2020, *Phys. Rev. D*, 102, 103506
- Alsing, J., Charnock, T., Feeney, S., & Wandelt, B. 2019, *MNRAS*, 488, 4440
- Aylor, K., Haq, M., Knox, L., Hezaveh, Y., & Perreault-Levasseur, L. 2020, *MNRAS*, 500, 3889
- BICEP2/Keck Array and Planck Collaborations. 2015, *Phys. Rev. Lett.*, 114, 101301
- Bruna, J. & Mallat, S. 2013, *IEEE transactions on pattern analysis and machine intelligence*, 35, 1872
- Bruna, J. & Mallat, S. 2019, *Mathematical Statistics and Learning*, 1, 257
- Cheng, S., Allys, E., Morel, R., Ménard, B., & Mallat, S. 2022, in prep.
- Cheng, S. & Ménard, B. 2021a, arXiv preprint arXiv:2112.01288
- Cheng, S. & Ménard, B. 2021b, *Monthly Notices of the Royal Astronomical Society*, 507, 1012
- Cheng, S., Ting, Y.-S., Ménard, B., & Bruna, J. 2020, *MNRAS*, 499, 5902
- Delabrouille, J., Betoule, M., Melin, J. B., et al. 2013, *A&A*, 553, A96
- Delouis, J.-M., Pagano, L., Mottet, S., Puget, J.-L., & Vibert, L. 2019, *Astronomy and Astrophysics - A&A*, 629, A38
- Delouis, J. M., Puget, J. L., & Vibert, L. 2021, *A&A*, 650, A82
- Durrer, R. 2015, *Classical and Quantum Gravity*, 32, 124007
- Eickenberg, M., Allys, E., Dizgah, A. M., et al. 2022, arXiv preprint arXiv:2204.07646
- Feng, C. & Holder, G. 2020, *ApJ*, 897, 140
- Górski, K. M., Hivon, E., Banday, A. J., et al. 2005, *ApJ*, 622, 759
- Greig, B., Ting, Y.-S., & Kaurov, A. A. 2022, *Monthly Notices of the Royal Astronomical Society*, 513, 1719
- Guth, A. H. 1981, *Phys. Rev. D*, 23, 347
- Hervías-Caimapo, C. & Huppenberger, K. M. 2022, *ApJ*, 928, 65
- Hildebrand, R. H., Kirby, L., Dotson, J. L., Houde, M., & Vaillancourt, J. E. 2009, *ApJ*, 696, 567
- Jeffrey, N., Boulanger, F., Wandelt, B. D., et al. 2022, *MNRAS*, 510, L1
- Kim, C.-G., Choi, S. K., & Flauger, R. 2019, *ApJ*, 880, 106
- Krachmalnicoff, N. & Puglisi, G. 2021, *ApJ*, 911, 42
- Kritsuk, A. G., Flauger, R., & Ustyugov, S. D. 2018, *Phys. Rev. Lett.*, 121, 021104
- Lagache, G., Béthermin, M., Montier, L., Serra, P., & Tucci, M. 2020, *A&A*, 642, A232
- Leistedt, B., McEwen, J. D., Vanderghynst, P., & Wiaux, Y. 2013, *Astronomy & Astrophysics*, 558, A128
- Linde, A. 1982, *Physics Letters B*, 116, 335
- LiteBIRD Collaboration, Allys, E., Arnold, K., et al. 2022, arXiv e-prints, arXiv:2202.02773
- Lopez-Radcenko, M., Delouis, J. M., & Vibert, L. 2021, *A&A*, 651, A65
- Mallat, S. 2012, *Communications on Pure and Applied Mathematics*, 65, 1331
- Mallat, S., Zhang, S., & Rochette, G. 2018, arXiv e-prints, arXiv:1810.12136
- Martínez-Solaache, G., Karacki, A., & Delabrouille, J. 2018, *MNRAS*, 476, 1310

- McEwen, J. D., Durastanti, C., & Wiaux, Y. 2018, *Applied and Computational Harmonic Analysis*, 44, 59
- McEwen, J. D., Leistedt, B., Büttner, M., Peiris, H. V., & Wiaux, Y. 2015, arXiv preprint arXiv:1509.06749
- McEwen, J. D., Wallis, C. G., & Mavor-Parker, A. N. 2021, arXiv preprint arXiv:2102.02828
- Morel, R., Rochette, G., Leonarduzzi, R., Bouchaud, J.-P., & Mallat, S. 2022, arXiv preprint arXiv:2204.10177
- Pelgrims, V., Ntormousi, E., & Tassis, K. 2022, *A&A*, 658, A134
- Petroff, M. A., Addison, G. E., Bennett, C. L., & Weiland, J. L. 2020, *ApJ*, 903, 104
- Planck Collaboration III. 2020, *A&A*, 641, A3
- Planck Collaboration Int. XLIV. 2016, *A&A*, 596, A105
- Planck Collaboration Int. XLVI. 2016, *A&A*, 596, A107
- Planck Collaboration Int. XXX. 2016, *A&A*, 586, A133
- Planck Collaboration IV. 2020, *A&A*, 641, A4
- Planck Collaboration V. 2020, *A&A*, 641, A5
- Planck Collaboration XI. 2020, *A&A*, 641, A11
- Planck Collaboration XII. 2020, *A&A*, 641, A12
- Planck Collaboration Int. XIX. 2015, *A&A*, 576, A104
- Regaldo Saint-Blancard, B., Allys, E., Boulanger, F., Levrier, F., & Jeffrey, N. 2021, *A&A*, 649, L18
- Regaldo-Saint Blancard, B., Levrier, F., Allys, E., Bellomi, E., & Boulanger, F. 2020, *A&A*, 642, A217
- Remazeilles, M., Delabrouille, J., & Cardoso, J.-F. 2011, *MNRAS*, 418, 467
- Ritacco, A., Boulanger, F., Guillet, V., et al. 2022, *A&A*, arXiv:2206.07671
- Saydjari, A. K., Portillo, S. K. N., Slepian, Z., et al. 2021, *ApJ*, 910, 122
- Thorne, B., Dunkley, J., Alonso, D., & Næss, S. 2017, *MNRAS*, 469, 2821
- Thorne, B., Knox, L., & Prabhu, K. 2021, *MNRAS*, 504, 2603
- Vacher, L., Aumont, J., Montier, L., et al. 2022, *A&A*, 660, A111
- Valogiannis, G. & Dvorkin, C. 2022a, arXiv preprint arXiv:2204.13717
- Valogiannis, G. & Dvorkin, C. 2022b, *Physical Review D*, 105, 103534
- Vansyngel, F., Boulanger, F., Ghosh, T., et al. 2017, *A&A*, 603, A62
- Zonca, A., Thorne, B., Krachmalnicoff, N., & Borrill, J. 2021, *The Journal of Open Source Software*, 6, 3783

## Appendix A: Additional figures

### Appendix A.1: Power spectra for $B$ -modes



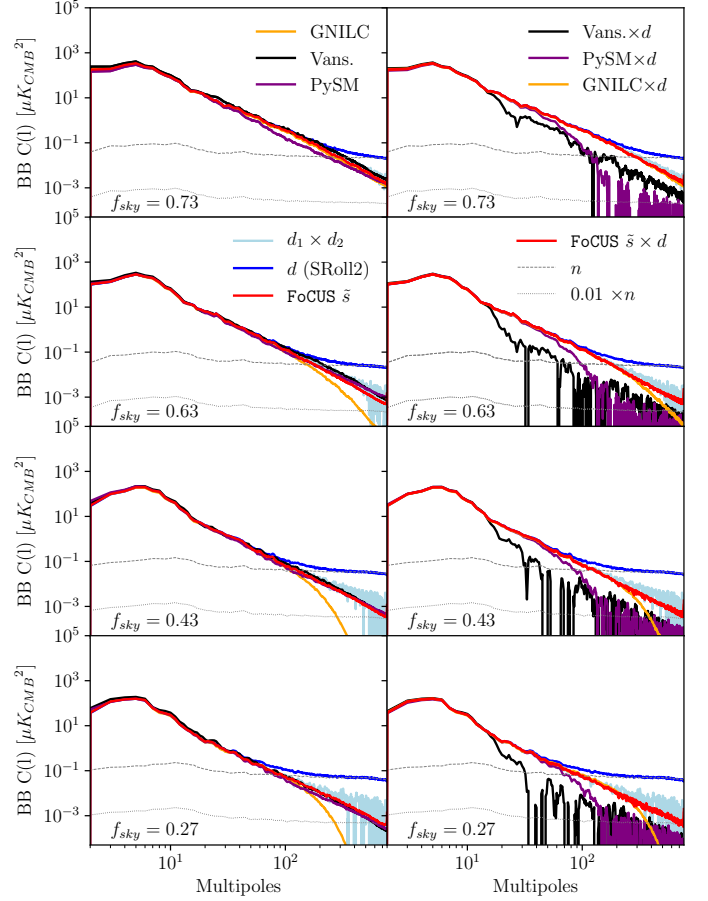
**Fig. A.1.** Power spectra of one realization for the FoCUS validation on mock data. The plots are the same as those in Fig.3 but for  $BB$  spectra.

Figure A.1 complements Fig. 3 by presenting  $BB$  power spectra of the FoCUS validation for one realization of the mock data. The signal-to-noise ratio is lower for  $BB$  than  $EE$  as the  $E$  to  $B$  power ratio for dust emission is about 2. Furthermore, the  $TB/TE$  power ratio is about one tenth, which decreases the impact of the loss term ( $\text{Loss}_3$ ) based on this correlation. For the mock data,  $\text{Loss}_3$  is fully ineffective because the Vansyngel model does not include the  $TB$  correlation. These effects combine to make FoCUS denoising more challenging. However, Fig. 3 shows a good consistency between the  $BB$  power spectra of the FoCUS and the input model maps for most multipoles. At very high Galactic latitudes (bottom right panel), the noisier part of the sky, the  $BB$  power spectrum of the FoCUS maps shows a small bias compared to that of the input maps, which reflects the limitation of our method when the signal-to-noise ratio is very low ( $< 1\%$ ).

Figure A.2 shows the same set of power spectra as in Fig. 8 but for  $BB$ . These plots demonstrate that the FoCUS results are consistent for  $BB$  and  $EE$ . The fact that both the  $EE$  and  $BB$  power spectra are properly retrieved demonstrates that the FoCUS maps keep the  $EE$  to  $BB$  power asymmetry.

### Appendix A.2: $S$ and $p$ plot for the mock data

Figure A.3 complements Fig. 10 by presenting the joint distribution of  $S$  and  $p$  for the Vansyngel model (left panel), one realization of the mock data (middle panel) and the result of the FoCUS denoising applied on the mock data (right panel). The eye-comparison of the three plots show that FoCUS considerably reduces the noise bias on the  $S$ – $p$  relation. We note that the analytical model of Planck Collaboration XII (2020) does not match the Vansyngel model for high  $p$  values. A similar shift between the analytical model and the data is observed for the Planck maps in the right panel of Fig. 10.



**Fig. A.2.** Power spectra (left column) and cross-power spectra (right column) for Galactic masks with  $f_{\text{sky}} = 0.27$  (bottom) to 0.73 (top). The plots are the same as those in Fig. 8 but for  $BB$  spectra.

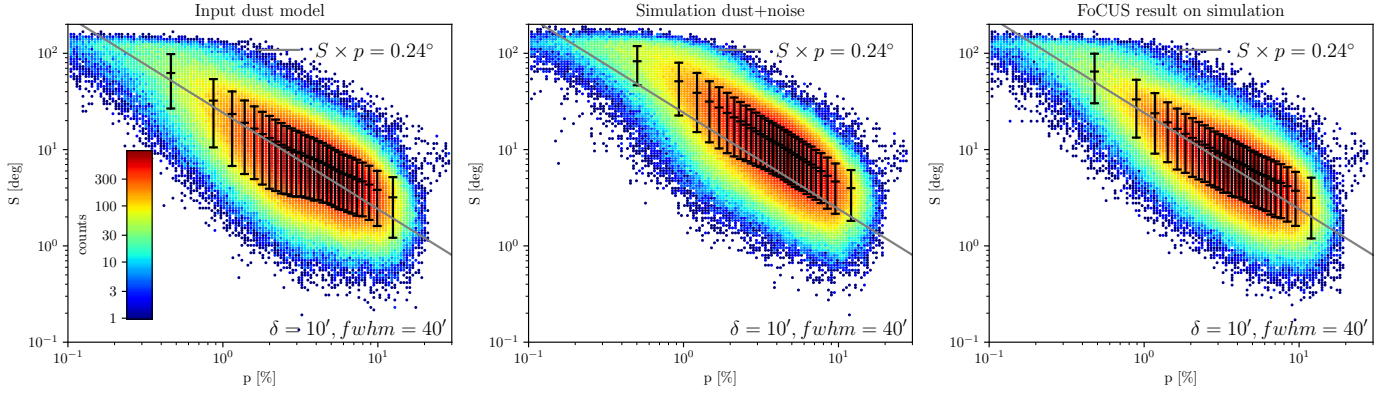


**Fig. A.3.** Same plot as in Fig. 10 for the Vansyngel model and the mock data. The figure shows the joint distribution of  $S$  and  $p$  for the Vansyngel model (left panel), one realization of the noisy mock data (middle panel) and the FoCUS denoised maps (right panel).